Article

Oligomerization Mechanism of Methylglyoxal Regulated by the Methyl Groups in Reduced Nitrogen Species: Implications for Brown Carbon Formation

Published as part of Environmental Science & Technology virtual special issue "Accelerating Environmental Research to Achieve Sustainable Development Goals".

Qiuju Shi,[||] Lei Gao,[||] Wenjian Li, Jiaxin Wang, Zhang Shi, Yixin Li, Jiangyao Chen, Yuemeng Ji,* and Taicheng An

Read Online

ACCESS | Metrics & More | Article Recommendations | Supporting Information

ABSTRACT: Uncertain chemical mechanisms leading to brown carbon (BrC) formation affect the drivers of the radiative effects of aerosols in current climate predictions. Herein, the aqueous-phase reactions of methylglyoxal (MG) and typical reduced nitrogen species (RNSs) are systematically investigated by using combined quantum chemical calculations and laboratory experiments. Imines and diimines are identified from the mixtures of methylamine (MA) and ammonia (AM) with MG, but not from dimethylamine (DA) with the MG mixture under acidic conditions, because deprotonation of DA cationic intermediates is hindered by the amino groups occupied by two methyl groups. It leads to N-heterocycle (NHC) formation in the MG + MA (MGM) and MG + AM (MGA) reaction systems but to N-containing chain oligomer formation in the MG + DA (MGD) reaction system. Distinct product formation is attributed to electrostatic attraction and steric hindrance, which are regulated by the methyl groups of RNSs. The light absorption and adverse effects of NHCs are also strongly related to the methyl groups of RNSs. Our finding reveals that BrC formation is mainly contributed from MG reaction with RNSs with less methyl groups, which have more abundant and broad sources in the urban environments.

KEYWORDS: methylglyoxal, reduced nitrogen species, methyl groups, aqueous-phase reaction mechanism, brown carbon formation
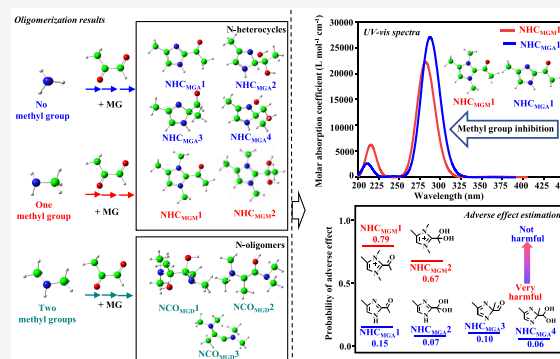
INTRODUCTION

Organic aerosols (OAs) have attracted widespread attention because of their threat to the climate, ecosystems, and human health. Exposure to OAs increases the risks of respiratory infections, adverse birth outcomes, and cardiorespiratory diseases.[1−6] OAs also influence the Earth−atmosphere system, such as changing cloud formation and precipitation processes, regulating the Earth's radiative balance, and reducing visibility and air quality.[7−9] Light-absorbing OAs, known as brown carbon (BrC), contribute to ~20% of aerosol-driven atmospheric heating.[10−14] One of the uncertain drivers for aerosol's radiative effects in current climate predictions is the incomplete understanding of the mechanism for BrC formation, chemical composition, and optical properties.[12,13] Especially, secondary BrC (SBrC) formation involves the complicated multiphase reactions among gas-phase, particulate, and cloud microdroplet constituents, increasing the uncertain components.[15−24]

The aqueous chemistry of methylglyoxal (MG) with reduced nitrogen species (RNSs) is believed to contribute significantly to SBrC formation.[16,24−30] MG is mainly yielded from photochemical oxidation of volatile organic compounds, with an estimated global source of 145 Tg a^{-1}.[31] In aqueous aerosol particles, MG exhibits small reactive exposure to submicrometer ammonium sulfate/sulfuric acid particles,[32−35] while rapid SBrC formation is detected in the MG and amine mixtures.[26,36] However, an increasing number of studies have revealed the high growth and rapid browning on ammonium/amine-containing particles exposed to continuous low levels of MG.[16,27,37,38] On the other hand, in a recent laboratory study, a slight yield of N-heterocycles (NHCs) is observed from the mixture of MG and dimethylamine (DA) under alkaline conditions.[26] However,

little information is available about the reaction of MG with DA in weakly acidic media characteristic of tropospheric conditions, i.e., on fine aerosols and cloud/fog droplets, to contribute to secondary organic aerosol (SOA) and BrC formation from biogenic and anthropogenic emissions. In addition, experimental studies have shown that the rapid photobleaching phenomenon of SBrC formed from the reactions of MG and ammonium sulfate/amines is related to its composition, and unclear SBrC components affect the evaluation of subsequent photobleaching.[37,38] Hence, SBrC formation from the aqueous chemistry of MG with RNSs and the effect of the methyl groups in RNSs on SBrC formation remain highly uncertain.

More importantly, the aqueous chemistry of MG has a wide range of impact on biological metabolism, and the regulation of the metabolism of small α-dicarbonyls in microorganisms is essential for biological life.[39,40] Such a process involves detoxification of MG formed from a normal part of microbial metabolism by a set of enzymes (i.e., glyoxalase system), with implications for diabetes, aging, and Alzheimer's disease as well as growth inhibition in different tumors.[40,41] On the other hand, previous studies have shown that SBrC chromophores, such as humic-like substances (HULIS), are also capable of inducing the oxidative stress effect, which has been unequivocally associated with respiratory inflammation, cardiovascular effects, and other adverse health effects.[42−46] The chemical composition of ∼30 major chromophores responsible for browning has been identified from the aqueous-phase reactions of MG with RNSs.[36,47−49] Therefore, due to the potential oxidative stress effect similar to HULIS, the adverse effects of BrC chromophores on human health are receiving increased attention.

Hence, we investigated the mechanisms of SBrC formation from the aqueous-phase reactions of MG with typical organic [i.e., methylamine (MA) and DA] and inorganic [i.e., ammonia (AM)] RNSs by combined quantum chemical calculations and kinetics modeling. The chemical mechanisms and kinetics of the three target reaction systems (MG + MA, MG + DA, and MG + AM) were established and elaborated. NHCs were identified by using theoretical and experimental approaches, and their UV−vis spectra were simulated using the time-dependent density functional theory. The effects of the methyl groups in RNSs on SBrC formation were discussed, and the implications of NHCs on potential adverse effects were assessed.

■ METHODOLOGY

Quantum Chemical and Kinetics Calculations. The electronic structures and energy caluclations were carried out using the Gaussian 09 program package.[50] All stationary points (including transition states, complexes, intermediates, and products) on the potential energy surface (SPE) were optimized using the hybrid density functional of the M06-2X method[51] with the 6-311G(d,p) basis set,[52] i.e., the M06-2X/6-311G(d,p) level, which has been proven to be a suitable method to simulate the geometric and energetic data in the aqueous-phase reactions because of its balance between the accuracy and computational efficiency.[41,53,54] The solvent effect was considered using the solvation model based on density (SMD) to simulate the aqueous environment.[55] At the same level, harmonic vibrational frequencies were calculated to verify the nature of the corresponding stationary point (transition state or minima) to provide the thermodynamic contributions to the Gibbs free energy. The well-defined transition state (TS) was searched by examining the stationary point (SP) using the TS keyword in

geometry optimization, while there was an absence of a TS if there was no energy exceeding the bond dissociation energy along the reaction coordinate.[56] The intrinsic reaction coordinate (IRC) calculation was performed to ensure that a given TS connects with the corresponding reactants and products, and pointwise potential curve (PPC) scanning was carried out to confirm a barrierless process (Figure S1). Several TSs in deprotonation pathways which cannot be searched at the level of M06-2X/6-311G(d,p) are identified at the M06-2X/6-311G(d) level. A detailed description is shown in the Supporting Information (SI). The characteristics for the natural charges of SPs were carried out by means of natural bond orbital (NBO) method.[57]

The single-point energy (SPE) was obtained by using the M06-2X method with a more flexible basis set 6-311++G(3df,3pd) based on the above geometric optimization. The dual-level potential profile along the reaction path was established at the M06-2X//M06-2X level. The dual-level approach was denoted as X//Y, where X is an SPE calculation at the M06-2X/6-311++G(3df,3pd) level and Y is the geometry optimized at the M06-2X/6-311G(d,p) level. To justify the performance of the M06-2X method for describing PES, the SPE calculation was also refined at the CCSD(T)/6-311++G-(2df,2pd) and CCSD(T)/aug-cc-pVTZ levels, i.e., coupled cluster approach with single and double substitutions including a perturbative estimate of connected triple substitutions with 6-311++G(2df,2pd) and aug-cc-pVTZ basis sets, respectively. As discussed in the SI and shown in Table S1, the M06-2X//M06-2X method is suitable for predicting the energies and represents a compromise between computational expense and accuracy.

The kinetic information for the reactions with well-defined TSs was calculated by using transition state theory (TST)[58−60] on the basis of the above PES. The solvent cage effect, free volume theory, and diffusion-limit effect were considered to the rate constants of bimolecular reactions.[61,62] The diffusion-limited rates were regarded as the rate constants of the barrierless processes because a reaction without TS is a diffusion-controlled process under an aqueous-phase solution. The computational details of kinetics are presented in the SI.

Using time-dependent density functional theory (TD-DFT) calculation[63−68] of the first 50 excited singlet electronic states, the electron transition energies were obtained at the M06-2X/6-311G(d,p) level based on the conformers with the lowest energies. The electron transition energies are corrected by a shift of −0.6 eV in order to directly compare the calculated spectra with experimental data,[68−70] and the breadth of 0.4 eV is applied to each excitation[68] to construct simulated absorption spectra. The calculated UV−vis absorption spectra were plotted by using the Multiwfn program[71] based on the above electronic transition energies. For comparison, the other two levels of B3LYP and WB97XD/6-311G(d,p) were also applied to calculate the electron transition energies (Figure S2). As discussed in the SI, UV−vis absorption spectra obtained at the M06-2X method are in better agreement with experimental data than other methods, indicating that the M06-2X method accurately provides reliable reference information for N-heterocycles.

The molecular planarity parameter (MPP) and span of deviation from the plane (SDP)[72] were evaluated via using the Multiwfn program[71] based on the above geometric optimization. MPP and SDP are complementary to each other, since the overall degree of deviation of the structure from a plane is reflected by MPP values, and the span of the structural deviation relative to the fitting plane is represented by SDP values.[72]
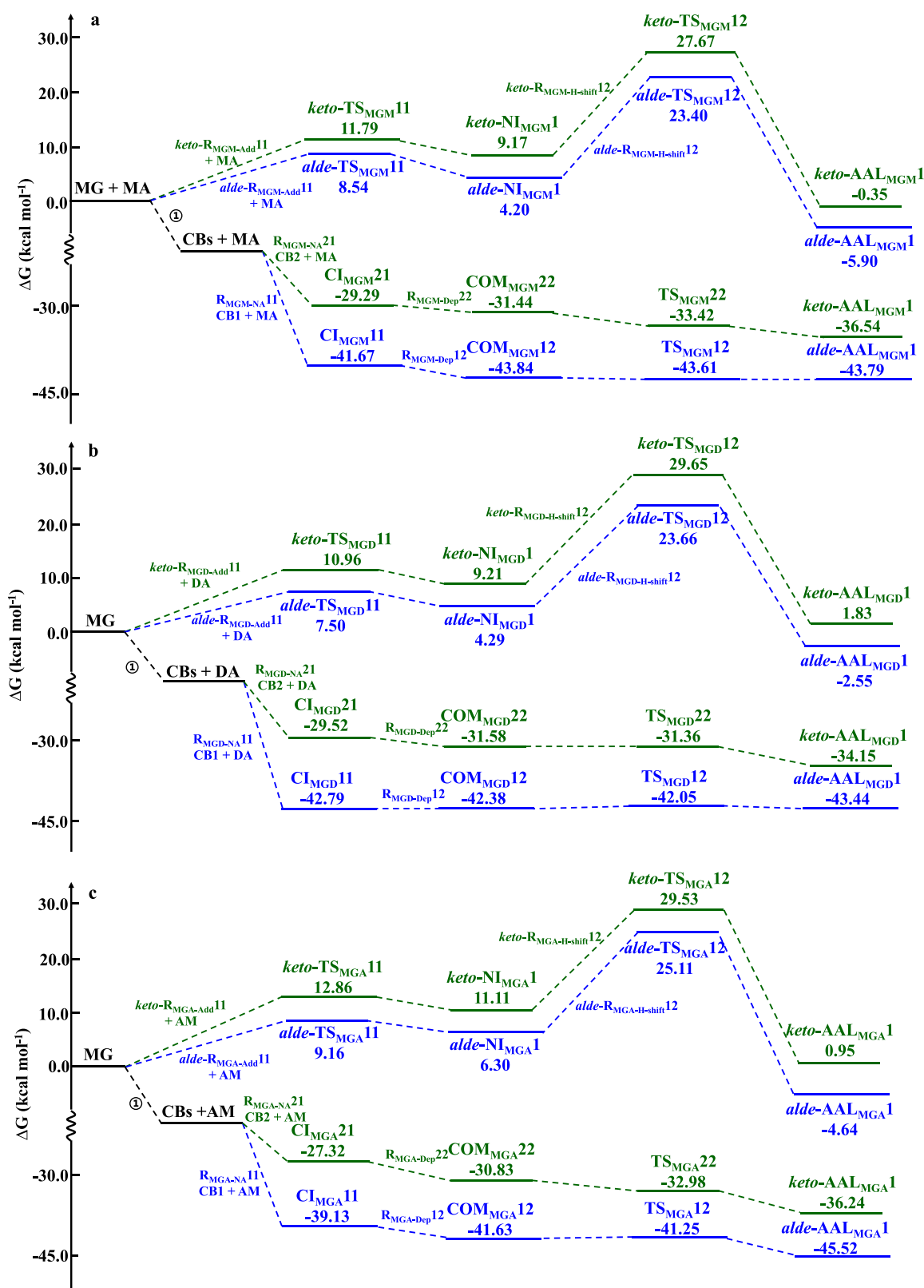
Figure 1. PESs of the direct nucleophilic addition and indirect association pathways of MG with (a) MA, (b) DA, and (c) AM (in kcal mol^{-1}). The number denotes the $\Delta G^{\ddagger}$ or ΔG_r for each reaction step. Step ① denotes the formation of CBs from ref 41.

Experimental Section. To identify the products of the model reaction systems, we performed laboratory measurements by the mixtures of MG + MA, MG + DA, and MG + AM. MG (40 wt % solution) and DA (40 wt % solution) chemicals were purchased from Aladdin (Shanghai, China). MA (40 wt % solution) was purchased from Damao Chemical Reagent Factory (Tianjin, China). Ammonium sulfate (AS, ≥99%) was purchased from Sigma-Aldrich. High-purity deionized water
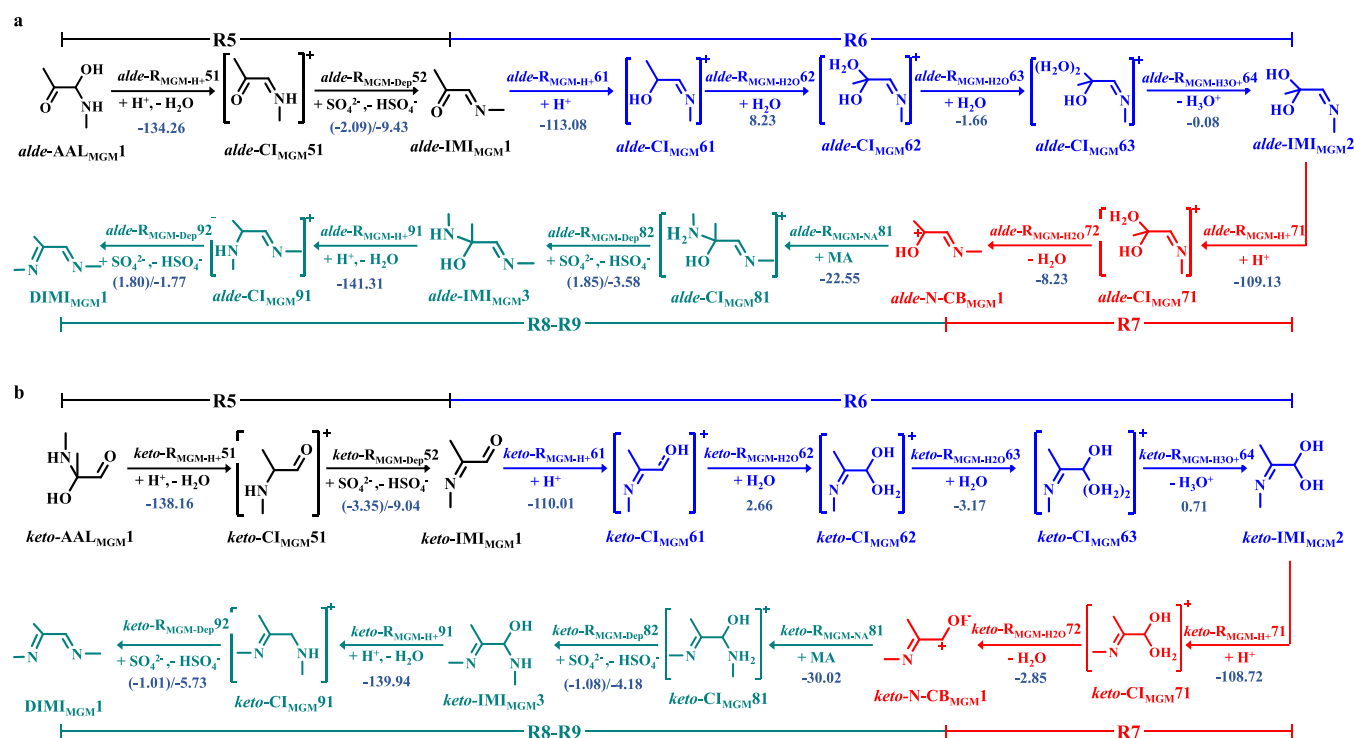
Figure 2. A schematic mechanism of four stepwise pathways involved in IMI and DIMI formation from *alde*- and *keto*-AAL$_{MGM}$1 (in kcal mol^{-1}). The number denotes the $\Delta G^{\ddagger}$ (in brackets) or ΔG_r for each reaction step, and all energies are relative to the corresponding reactants.

(18.2 MΩ·cm; Millipore Corp., USA) was used for dissolution and dilution. MA and DA were acidified with a diluted sulfuric acid of 20% to simulate atmospheric acidic aqueous conditions. For the MG + MA or MG + DA mixture, aqueous MG was combined with acidified RNS with a final concentration of 1 M for each reactant in the volumetric flask, while the MG + AM mixture was prepared by adding AS to aqueous MG (in ultrapure water). Each mixed solution was finally regulated to the initial pH values of 3, 4, and 5 (denoted as pH 3, 4, and 5), respectively, with sodium hydroxide solution. The pH value was measured with an Ohaus Starter 3100 pH meter (Ohaus corporation). Three parallel samples were required for each mixture mentioned above, and each sample was then transported into a brown vial for 3 days under dark conditions. Before mass spectrometry, all samples were diluted by a factor of 1000 followed by syringe filtration. The filters were injected into brown chromatography injection bottles, avoiding photolysis of the products. Ultraperformance liquid chromatography coupled to hybrid quadrupole-exactive orbitrap mass spectrometry (UPLC-Q-Orbitrap HRMS, Thermo Scientific, USA)[73] was employed to obtain structural and UV−vis data of products. The selected chromatographic column was a Hypersil GOLD C18 (100 × 2.1 mm, 1.9 μm). The eluents were ultrapure water (eluent A) and acetonitrile (eluent B), and the injection volume was 1 μL. The flow rate of the mobile phase was 0.25 mL min^{-1} with a gradient described as follows: first, starting with 2% B for 2 min, increasing to 95% B at 15 min, isocratic elution for 3 min, then decreasing to 2% B in 0.1 min, and finally maintaining 2% B for 20 min. UV−vis spectra (200−500 nm) were measured using a photodiode array (PDA) detector. Mass spectrometry detectors were equipped with a HESI source and set according to the following parameters: 4 kV spray voltage, 30 units of sheath gas flow, 10 units of auxiliary gas flow, 320 °C capillary temperature, and 350 °C auxiliary gas heater temperature. MS

mode was set with a scan range of 50−750 *m/z* with a resolution of 70000. The PDA and HRMS data were both processed with Xcalibur 4.1 software (Thermo Scientific) to obtain the UV−vis absorption spectra and mass spectra. MS analysis was used for all products with a weight error of less than 5 ppm compared with the theoretical mass to identify the structures.

RESULTS AND DISCUSSION

RNS-Initiated Reactions of MG. The calculated PESs for the possible pathways of RNS-initiated reactions of MG are presented in Figures 1 and S3. The initial reactions of MA, DA, and AM with MG occur via two distinct pathways: direct nucleophilic addition of MG by RNSs and indirect association mediated by other species. The nomenclature for each pathway (R_{X-Y}) is established for the convenience of the following discussion, where X denotes the three target reaction systems, i.e., MGM (MG + MA), MGD (MG + DA), and MGA (MG + AM), and Y represents an elementary reaction, i.e., direct nucleophilic addition, indirect association, etc. The optimized geometries of all SPs in the direct nucleophilic addition and indirect association pathways are shown in Figures S4 and S5.

As shown in Figure 1, the activation energy ($\Delta G^{\ddagger}$) and reaction energy (ΔG_r) of the direct nucleophilic addition depend on the addition of the three target RNSs to the aldehyde (*alde*-R_{X-Add}) or ketone (*keto*-R_{X-Add}) group of MG. For the three reaction systems, the transition states (*alde*- and *keto*-TS$_X$1s) of the *alde*- and *keto*-R_{X-Add} pathways are identified, with their $\Delta G^{\ddagger}$ values ranging from 7.50 to 12.86 kcal mol^{-1}. The formation of *alde*- and *keto*-neutral intermediates (*alde*- and *keto*-NI$_X$1s) is an endothermic process, with the ΔG_r values ranging from 4.20 to 11.11 kcal mol^{-1}. The subsequent intramolecular H shifts of *alde*- and *keto*-NI$_X$1s (i.e., *alde*- and *keto*-$R_{X-H-shift}$12 pathways in Figure 1) also occur with large $\Delta G^{\ddagger}$ values from 18.42 to 20.44 kcal mol^{-1}, leading to *alde*- and *keto*-amino alcohols (i.e., *alde*-
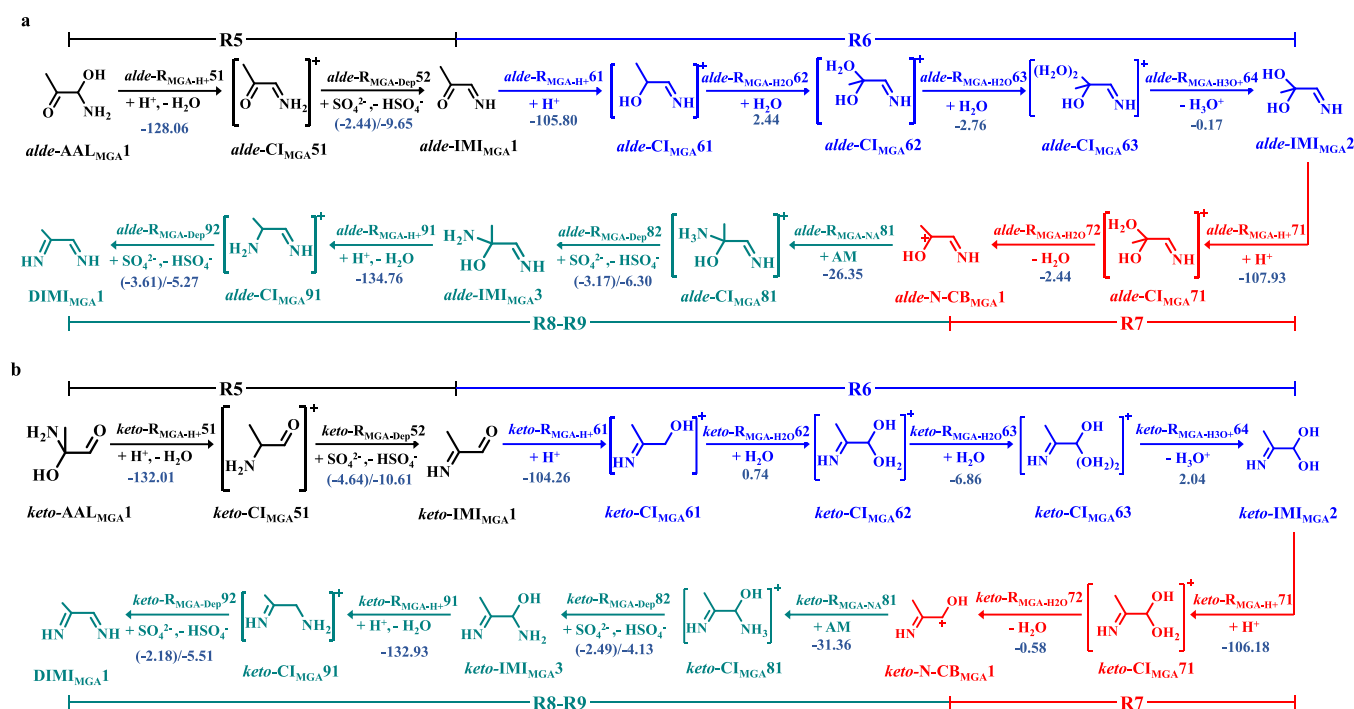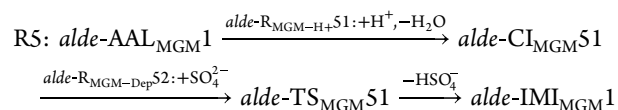
Figure 3. A schematic mechanism of four stepwise pathways involved in IMI and DIMI formation from *alde-* and *keto-*AAL$_{MGA}$1 (in kcal mol^{-1}). The number denotes the $\Delta G^{\ddagger}$ (in brackets) or ΔG_r for each reaction step, and all energies are relative to the corresponding reactants.

and *keto-*AAL$_X$1s), respectively. The large activation barriers imply the unfavorable formation of *alde-* and *keto-*AAL$_X$1s via direct nucleophilic addition pathways.

For the indirect association pathways, four first-generation carbenium ions (CB1 and CB4) are selected to mediate the association reactions of MG with RNSs. CBs are broadly and rapidly formed without barrier from MG solution,[27,41] implying that there exist abundant CBs to engage in the formation and propagation of BrC. According to a previous study,[41] first-generation CBs are barrierlessly formed via protonation and hydration of MG to yield diols and tetrol and subsequent protonation of diols and tetrol. Herein, four first-generation CBs (CB1−4) are chosen as the model of CBs. The CB-mediated association involves two-step reactions (Figures 1 and S3), i.e., nucleophilic addition (R$_{X-NA}$) and then deprotonation (R$_{X-Dep}$). Contrary to the direct nucleophilic addition pathways, PESs along the indirect association pathways illustrate that all pathways involved in the R$_{X-NA}$ and R$_{X-Dep}$ pathways are barrierless or possess small activation barriers (Figures 1 and S3). For example, the nucleophilic addition of MA to CB1 (R$_{MGM-NA}$1) occurs with strong exothermicity ($\Delta G_r = -41.67$ kcal mol^{-1}), yielding the cationic intermediate (CI$_{MGM}$11). The subsequent deprotonation of CI$_{MGM}$11 (R$_{MGM-Dep}$12) proceeds with a negative $\Delta G^{\ddagger}$ value of -1.94 kcal mol^{-1} to form *alde-*AAL$_{MGM}$1. Prior to the TS, there is a prereactive complex (*alde-*COM$_{MGM}$12), whose energy is -2.17 kcal mol^{-1} lower than that of the corresponding reactants. The kinetics data listed in Tables S2−S5 show that the calculated rate constants of all indirect association pathways are in the range of ∼10^9 M^{-1} s^{-1}, which are 2−6 orders of magnitude larger than those of the pathways involved in the direct nucleophilic addition. In summary, the small activation energies and large rate constants indicate that the CB-mediated association reactions of MG and RNSs are thermodynamically and kinetically feasible for the formation of amino alcohols (i.e., *alde-* and *keto-*AALs).
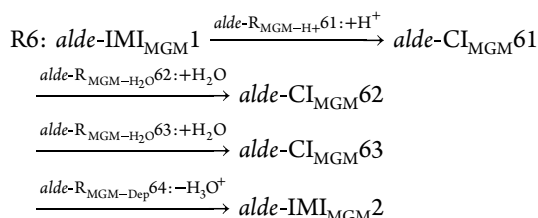
Subsequent Oligomerization of AALs in H$_2$SO$_4$ Solution. As discussed above, *alde-* and *keto-*AALs are the main products of the initial reactions of MG with RNSs. Figures 2, 3, and S6 show the subsequent reaction pathways of *alde-* and *keto-*AAL$_X$1s, as the model of AALs, in the three reaction systems. The subsequent oligomerization in H$_2$SO$_4$ solution involves two stages, i.e., diimine (DIMI) and NHC formation. Herein, the pathways involved are by default barrierless processes unless otherwise stated because most pathways are proven to be barrierless (Figure S1b) or to possess small or negative activation energies. The optimized geometries of all SPs involved in the oligomerization of *alde-* and *keto-*AAL$_X$1s are presented in Figures S7−S11.

Formation of Imines and Diimines. From the viewpoint of quantum chemical results (see the SI for a detailed discussion and Figure S6), no imines (IMIs) and DIMIs are formed in the MG + DA reaction system because of the structural characteristics of *alde-* or *keto-*AAL$_{MGD}$1, since their amino groups are occupied by two methyl groups. However, for the MG + MA and MG + AM reaction systems, the amino groups of *alde-* or *keto-*AAL$_{MGM}$1 and AAL$_{MGA}$1 provide deprotonation sites to form IMIs and DIMIs (Figures 2 and 3). For the MG + MA reaction system, the multistep processes of *alde-*AAL$_{MGM}$1 to *alde-*IMI$_{MGM}$1 are described as follows (Figure 2a):

R5: $alde\text{-}AAL_{MGM}1 \xrightarrow{alde\text{-}R_{MGM-H+}51:+H^+,-H_2O} alde\text{-}CI_{MGM}51$

$\xrightarrow{alde\text{-}R_{MGM-Dep}52:+SO_4^{2-}} alde\text{-}TS_{MGM}51 \xrightarrow{-HSO_4^-} alde\text{-}IMI_{MGM}1$
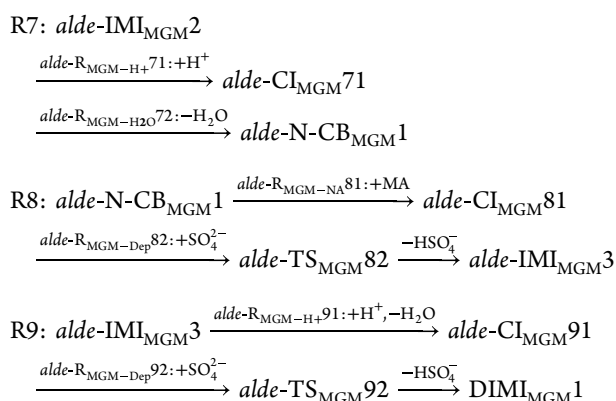
As shown in Figure S7a, the C−O bond of *alde-*AAL$_{MGM}$1 is broken to 2.58 Å, as protonation occurs in the alcohol hydroxyl group, implying the one-step reaction of *alde-*CI$_{MGM}$51 formation. The ΔG_r value of the *alde-*R$_{MGM-H+}$51 pathway is -134.26 kcal mol^{-1}, which includes the proton affinity of water with -110.87 kcal mol^{-1}.[41,54] The subsequent deprotonation of *alde-*CI$_{MGM}$51 proceeds via a prereactive complex (*alde-*

$COM_{MGM}52$) prior to the TS ($alde$-$TS_{MGM}52$), with a $\Delta G^{\ddagger}$ value of -2.09 kcal mol^{-1}, forming $alde$-$IMI_{MGM}1$. An intermolecular isomerization pathway from $alde$-$IMI_{MGM}1$ to $alde$-$IMI_{MGM}2$ is observed, owing to the presence of a carbonyl group in $alde$-$IMI_{MGM}1$.

R6: $alde$-$IMI_{MGM}1 \xrightarrow{alde\text{-}R_{MGM-H+}61:+H^+} alde$-$CI_{MGM}61$

$\xrightarrow{alde\text{-}R_{MGM-H_2O}62:+H_2O} alde$-$CI_{MGM}62$

$\xrightarrow{alde\text{-}R_{MGM-H_2O}63:+H_2O} alde$-$CI_{MGM}63$

$\xrightarrow{alde\text{-}R_{MGM-Dep}64:-H_3O^+} alde$-$IMI_{MGM}2$

All pathways (such as protonation, hydration, and deprotonation) involved in the R6 process have successively decreasing ΔG_r values (i.e., from 8.23 to -113.08 kcal mol^{-1}; Figure 2a). $Alde$-$IMI_{MGM}2$ undergoes protonation and dehydration to form a N-containing CB ($alde$-N-$CB_{MGM}1$; R7). The nucleophilic attack of $alde$-N-$CB_{MGM}1$ by MA forms $DIMI_{MGM}1$ via stepwise processes (R8 and R9).

R7: $alde$-$IMI_{MGM}2$

$\xrightarrow{alde\text{-}R_{MGM-H+}71:+H^+} alde$-$CI_{MGM}71$

$\xrightarrow{alde\text{-}R_{MGM-H_2O}72:-H_2O} alde$-N-$CB_{MGM}1$

R8: $alde$-N-$CB_{MGM}1 \xrightarrow{alde\text{-}R_{MGM-NA}81:+MA} alde$-$CI_{MGM}81$

$\xrightarrow{alde\text{-}R_{MGM-Dep}82:+SO_4^{2-}} alde$-$TS_{MGM}82 \xrightarrow{-HSO_4^-} alde$-$IMI_{MGM}3$

R9: $alde$-$IMI_{MGM}3 \xrightarrow{alde\text{-}R_{MGM-H+}91:+H^+,-H_2O} alde$-$CI_{MGM}91$

$\xrightarrow{alde\text{-}R_{MGM-Dep}92:+SO_4^{2-}} alde$-$TS_{MGM}92 \xrightarrow{-HSO_4^-} DIMI_{MGM}1$

As shown in Figure 2a, the ΔG_r value of the $alde$-$R_{MGM-NA}81$ pathway is -22.55 kcal mol^{-1}, forming $alde$-$CI_{MGM}81$. Subsequent deprotonation of $alde$-$CI_{MGM}81$ ($alde$-$R_{MGM-Dep}82$) also possesses a low $\Delta G^{\ddagger}$ value of 1.85 kcal mol^{-1}. Subsequently, $alde$-$IMI_{MGM}3$ repeats protonation accompanied by dehydration, and deprotonation to form $DIMI_{MGM}1$, with a total ΔG_r value of -143.08 kcal mol^{-1}. Similar to $alde$-$AAL_{MGM}1$, $keto$-$AAL_{MGM}1$ also reacts via protonation, hydration, deprotonation, and isomerization to yield $keto$-IMI_{MGM}s ($keto$-$IMI_{MGM}1$, $keto$-$IMI_{MGM}2$, and $keto$-$IMI_{MGM}3$) and $DIMI_{MGM}$ ($DIMI_{MGM}1$; see the detailed discussion in the SI). Totally, six IMI_{MGM}s and one $DIMI_{MGM}1$ are formed in the MG + MA reaction system.
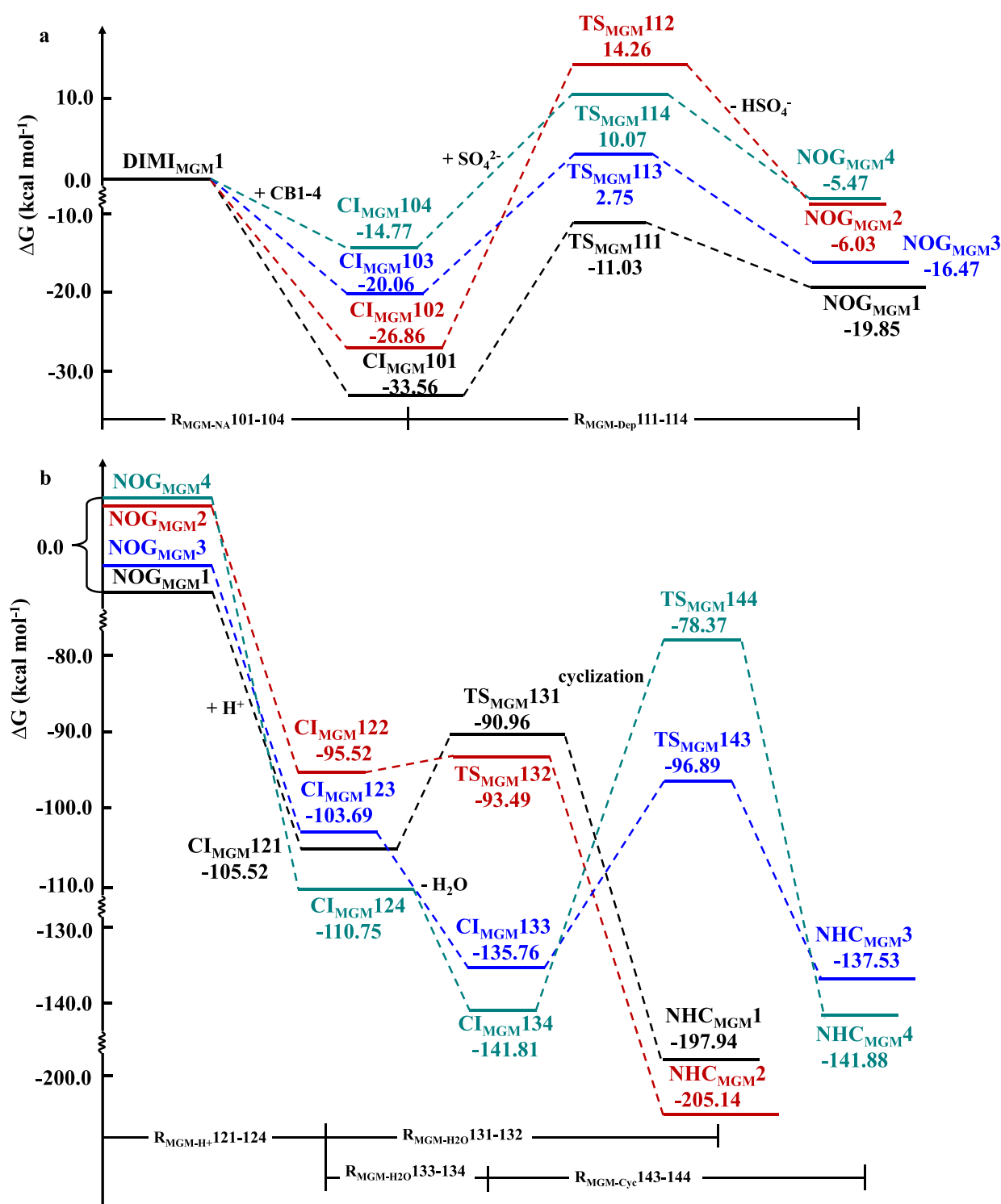
For the MG + AM reaction system, the formation of IMI_{MGA}s and $DIMI_{MGA}$s also proceeds via the following four vital steps (see the SI for a detailed discussion and Figure 3): (i) protonation of $AAL_{MGA}1$ at the alcohol hydroxyl group to yield IMI_{MGA}s; (ii) isomeric conversion of IMI_{MGA}s via protonation, hydration, and deprotonation; (iii) protonation and dehydration of IMI_{MGA}s to N-CB_{MGA}s; and (iv) formation of $DIMI_{MGA}1$ by the association reactions of N-CB_{MGA}s with AM. Six IMI_{MGA}s and one $DIMI_{MGA}1$ are formed in the MG + AM reaction system. According to the previous studies, the fate of AAL is dependent on the competition between R5 (protonation and deprotonation to yield IMIs) and R10 (nucleophilic addition with CBs and deprotonation to form neutral intermediate (NIs)) pathways (Figure S12). The ΔG_r value of the $alde$-$R_{MGA-H+}51$ pathway is -128.06 kcal mol^{-1}, and the $\Delta G^{\ddagger}$ value of the $alde$-$R_{MGA-Dep}52$ pathway is -2.44 kcal mol^{-1}, comparable

with the ΔG_r value of -32.93 kcal mol^{-1} ($alde$-$R_{MGA-NA}101$ pathway) and $\Delta G^{\ddagger}$ value of -6.88 kcal mol^{-1} ($alde$-$R_{MGA-Dep}102$ pathway). Hence, competition reaction pathways for the AAL are equally accessible. In summary, deprotonation of N-containing cationic intermediates at the amino groups is initiated by SO_4^{2-} via a small or negative activation energy, implying an approximately barrierless process for this type of deprotonation. The rate constants, presented in Table S6, are all in the range of $\sim10^9$ M^{-1} s^{-1} for the MG + MA and MG + AM reaction systems. Combined with previous studies,[26,54] we can infer that the formation of IMIs and DIMIs in the two reaction systems is regulated by electrostatic attraction and steric hindrance.

N-heterocycle Formation. Oligomerization of DIMIs starts from the nucleophilic addition with CBs, and Figures 4 and S13 describe PESs of the association reactions of DIMIs with CB1−4, leading to the formation of various N-containing oligomers (NOGs) and NHCs. For the MG + MA reaction system, the N2 atom of $DIMI_{MGM}1$ is more susceptible to attack by CBs because of its more negative natural charge (-0.47 e) relative to the N1 atom (-0.44 e), yielding four different CIs ($CI_{MGM}101−104$). As shown in Figure S14, there is a smaller steric hindrance and stronger electrostatic attraction between $DIMI_{MGM}1$ and CB1. Therefore, the $R_{MGM-NA}101$ pathway possesses a larger exothermicity (-33.56 kcal mol^{-1}) than those of $R_{MGM-NA}102−104$ pathways, which is sufficient to overcome the activation barrier (22.53 kcal mol^{-1}) to deprotonate $CI_{MGM}101$ to yield $NOG_{MGM}1$. The subsequent protonation of $NOG_{MGM}1$ ($R_{MGM-H+}121$) has a large exothermicity (-105.52 kcal mol^{-1}) for the cyclization reaction, leading to the formation of $NHC_{MGM}1$. Hence, the formation of $NHC_{MGM}1$ by the association of $DIMI_{MGM}1$ with CB1 is favorable. This is also explained by the more accessible formation of CB1.[41] As shown in Figure S15a, $NHC_{MGM}2$ is formed by the intermolecular isomerization of $NHC_{MGM}1$ ($R_{MGM}15$), and $NHC_{MGM}1$ and $NHC_{MGM}2$ are imidazolium cations without nucleophilic and deprotonated sites.

For the MG + AM reaction system, it also proceeds via the nucleophilic addition of $DIMI_{MGA}1$ by CBs to form NOG_{MGA}s, followed by the cyclization of NOG_{MGA}s to yield NHCs (Figure S13). However, the following two distinct differences are observed in the MG + AM and MG + MA reaction systems: (i) the nucleophilic addition pathways of $DIMI_{MGA}1$ with CB1−4 possess the negative $\Delta G^{\ddagger}$ values and (ii) the cyclization pathways of $NOG_{MGA}1−4$ yield four unstable CIs ($CI_{MGA}151−154$) rather than NHCs. Nonionic NHCs ($NHC_{MGA}1−4$) in the MG + AM reaction system are formed by deprotonation of $CI_{MGA}151−154$ because of the presence of additional deprotonation sites. Also, $NHC_{MGA}1$ and $NHC_{MGA}3$ can be isomerized to form $NHC_{MGA}2$ and $NHC_{MGA}4$ (Figure S15b), via a pathway analogous to $R_{MGM}15$. Considering the more favorable formation of CB1 and CB2 relative to CB3 and CB4,[41] the formation of $NHC_{MGA}1$ and $NHC_{MGA}3$ from the association of $DIMI_{MGA}1$ with CB1 and CB2 is more accessible than that of $NHC_{MGA}2$ and $NHC_{MGA}4$ from the association of $DIMI_{MGA}1$ with CB3 and CB4.

In summary, all pathways involved in nucleophilic addition and cyclization in the MG + AM reaction system have lower $\Delta G^{\ddagger}$ values than the corresponding pathways in the MG + MA reaction system (Figures 4 and S13), whereas the analogous nucleophilic addition cannot occur in the MG + DA reaction system because of the absence of DIMI formation (Figure 5a). This indicates that NHC formation from the MG + MA reaction

Figure 4. PESs of the association reactions of DIMI$_{MGM}$1 with CB1−4 to form (a) NOG$_{MGM}$s and then (b) NHC$_{MGM}$s (in kcal mol^{-1}). The number denotes the $\Delta G^{\ddagger}$ or ΔG_r for each reaction step.

system is weaker than that from the MG + AM reaction system since there exist more methyl groups in MA. On the other hand, the formation of NHCs from the MG + MA reaction system is more dependent on the content of atmospheric aerosols than that from the MG + AM reaction system because sulfate ions are more accessible in the latter reaction. Hence, the formation of NHCs is inhibited with the increasing number of the methyl groups in RNSs.

Chemical Composition. We combined mass spectra with extracted ion chromatograms (EICs) to analyze the chemical composition of the MG + MA, MG + DA, and MG + AM reaction systems using UPLC-Q-Orbitrap HRMS. The identified N-heterocyclic products reveal NHC$_{MGM}$1−2 (m/z = 153.10 and 171.11) and NHC$_{MGA}$1−4 (m/z = 125.07 and 143.08; Figures 5b and S16a and Table S7), encompassing all six energetically favorable NHCs identified from our theoretical calculations (Figures 4 and S13) in the MG + MA and MG + AM
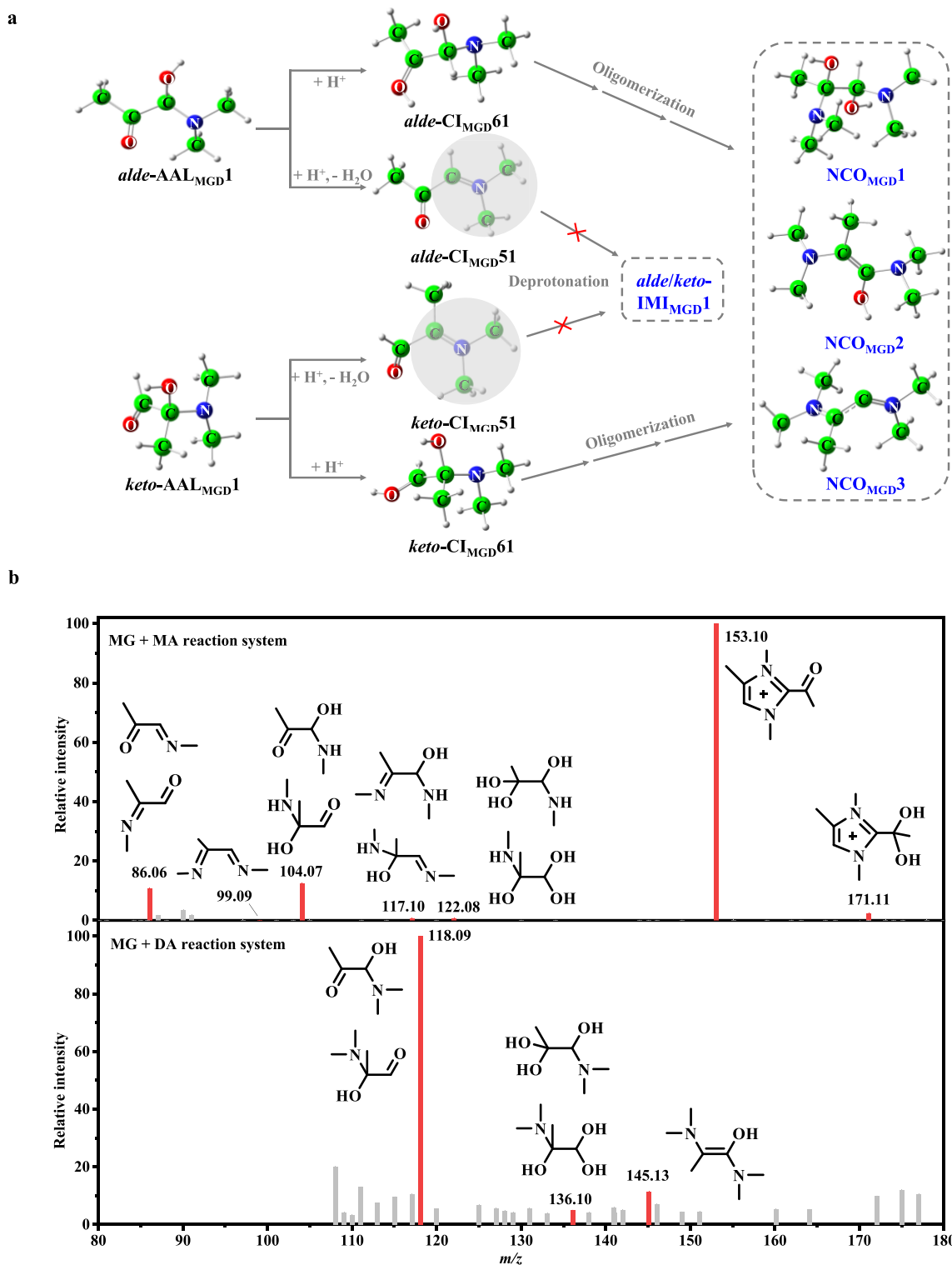
Figure 5. (a) Schematic subsequent oligomerization to form N-containing chain oligomers in the MG + DA reaction system. (b) The mass spectra monitoring of key intermediates and N-heterocycles for the MG + MA and MG + DA mixtures (pH = 4). The red lines represent the peaks of the products in our work, and gray lines represent the residual peaks.

reaction systems. $NHC_{MGM}1-2$ and $NHC_{MGA}1-4$ are further identified using the corresponding EICs, which exhibit obvious peaks when eluted within 4 min (Figures S17a and S17c). The most abundant NHCs (i.e., m/z = 153.10 for $NHC_{MGM}1$ in the MG + MA reaction system and m/z = 125.07 for $NHC_{MGA}1$ and $NHC_{MGA}3$ in the MG + AM reaction system) correspond to the $R_{MGM}101-131$, $R_{MGA}111-161$, and $R_{MGA}113-163$ pathways

mentioned above in our theoretical work. For the MG + DA reaction system, no peak is observed at m/z = 99.07 and 112.10, implying that IMIs and DIMIs are not formed under acidic conditions, in agreement with the analysis from our theoretical results. The product (m/z = 145.13) exhibits no peak in its EIC, but it probably corresponds to the N-containing chain oligomer
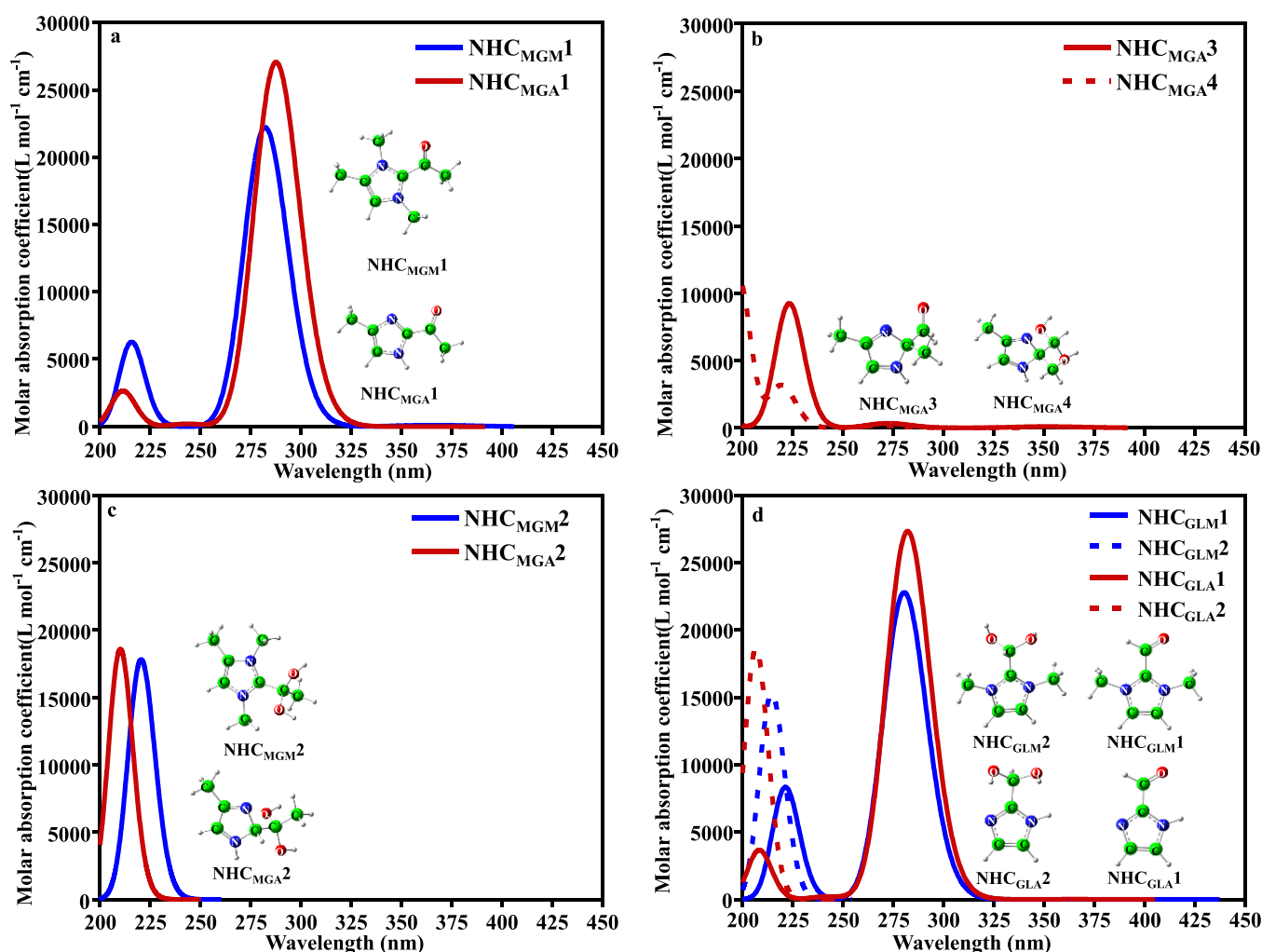
Figure 6. Molar absorption coefficients of 10 N-heterocycles in the MG + RNSs and GL + RNSs reaction systems. The data of the GL + MA and GL + AM reaction systems were obtained from ref 54.

NCO$_{MGD}$2 combined with our calculated results that the N-containing chain oligomer is the dominant product.

Analysis of UV−Vis Light Absorption. To evaluate the impact of NHCs on the atmosphere, we investigated the UV−vis absorption spectra of the main NHCs (i.e., NHC$_{MGM}$s and NHC$_{MGA}$s), and the corresponding UV−vis absorption spectra are shown in Figure 6a−c. All target NHCs exhibit absorptivity in the region from 200 to 325 nm. The NHCs with a keto group in the side chain (i.e., NHC$_{MGM}$1 and NHC$_{MGA}$1) exhibit stronger absorption in the region from 260 to 325 nm, corresponding to the $n \rightarrow \pi^*$ electronic transition, implying that these compounds contribute to significant BrC absorption in the target reaction systems. To visualize the change in the electron density upon absorption, a natural transition orbital (NTO) analysis was performed (Figure S18), including the highest-occupied (HOTO) and lowest-unoccupied transition orbitals (LUTO), corresponding to a one-electron representation of the change in the electron density from the ground to the excited state. As shown in Figure S18, the HOTOs of NHC$_{MGM}$1 and NHC$_{MGA}$1 are mainly localized on the carbonyl O atoms, whereas the LUTOs of NHC$_{MGM}$1 and NHC$_{MGA}$1 are contributed by C−O bonds adjacent to the imidazole ring, exhibiting a contribution from the lone pair of O atoms to the π^* orbital of the C−O bonds ($n \rightarrow \pi^*$ electronic transition). For NHC$_{MGA}$3 and NHC$_{MGA}$4, their absorption peaks become blue-shifted into the region from 200 to 250 nm, corresponding to the $\pi \rightarrow \pi^*$ electronic transition, attributable to the structural characteristics of methyl-steric hindrance (Figure S18). The HOTOs that are mainly located on the double bonds ($-$C$=$N$-$) of the imidazole ring and the LUTOs that are mostly focused on the imidazole ring exhibit the $\pi \rightarrow \pi^*$ electronic transition (Figure S18). The $\pi \rightarrow \pi^*$ excitation centered at 223 and 219 nm contributes to the absorption tail into the visible spectrum, also resulting in light absorption into the BrC region. However, their characteristic absorption peaks are weaker than that of NHC$_{MGA}$1 because of the weaker planarity and larger steric hindrance of NHC$_{MGA}$3 and NHC$_{MGA}$4, leading to a decrease in the conjugative effect (Figure S19). However, when the carbonyl groups of NHC$_{MGM}$1 and NHC$_{MGA}$1 are substituted by two hydroxyl groups (corresponding to NHC$_{MGM}$2 and NHC$_{MGA}$2), the maximum absorption peaks are centered at 221 and 210 nm, respectively, with no absorption observed beyond 265 nm, implying that these two compounds cannot contribute to any observed absorbance in the BrC region due to the lack of the conjugative degree. Hence, the light absorption of NHCs is regulated by both methyl groups and the conjugative effect, and NHC$_{MGM}$1 and NHC$_{MGA}$1 with strong planarity in the side chain are significant contributors to light absorption in the BrC region.

To provide insights into the abundance and contribution to the total absorptivity, the total ion chromatogram (TIC), UPLC-PDA, and UV−vis spectrum in the MG + AM mixture is measured in the range of 200−500 nm using a PDA detector (Figure S20). As discussed in the SI, $NHC_{MGA}1$ is found in high abundance in the BrC region and exhibits a strong light absorption in the range of 260 to 325 nm, with a maximum absorption peak at 280 nm. However, for the other species in the MG + AM mixture, no obvious light absorption is observed at ∼280 nm. This indicates that $NHC_{MGA}1$ is the main contributor to total light absorption in the BrC region, which is in agreement with the theoretical results mentioned above. It implies that our theoretical results of obvious light absorption for $NHC_{MGM}1$ and no light absorption for $NHC_{MGM}2$ in the BrC region are expected to reasonably predict the main contributor to the light absorption in the MG + MA reaction system although the UV−vis spectra of the individual chromophore cannot be separated completely by UPLC.

Adverse Health Effect of N-Heterocycles. To estimate the adverse effects of NHCs on human health, the probability of adverse effects (PAE) of NHCs on the lungs is evaluated using the module of health effects in the ACD/Percepta platform,[74,75] which has been applied and proven to be an effective module to predict the probabilities of organ-specific adverse effects in the therapeutic dose range.[74,76] The PAE values of NHCs on the human body are obtained based on the data for >100 000 compounds collected from chronic, subchronic, acute toxicity, and carcinogenicity studies, with adverse effects reported on particular human body system. The PAE values quantify whether the products have adverse effects on the human body, and in the range from 0 to 1.[74] A smaller PAE value represents a weaker adverse health effect. The PAE values of NHCs in the MG + MA and MG + AM reaction systems are shown in Figure S21.

The PAE values of $NHC_{MGM}1$ and $NHC_{MGM}2$ are 0.79 and 0.67 in the lungs, respectively, while those of $NHC_{MGA}1$, $NHC_{MGA}2$, $NHC_{MGA}3$, and $NHC_{MGA}4$ are 0.15, 0.07, 0.10, and 0.06, respectively. The PAE values of NHCs in the MG + MA reaction system are 6−7 times larger than those of NHCs in the MG + AM reaction system, suggesting stronger adverse effects of NHCs on human health in the MG + MA reaction system than in the MG + AM reaction system. To further evaluate the adverse effects of NHCs on human health, the PAE values in the lungs for the four additional NHCs ($NHC_{GLM}1$, $NHC_{GLM}2$, $NHC_{GLA}1$, and $NHC_{GLA}2$) in the GL + MA and GL + AM reaction systems are also predicted and are presented in Figure S21. The PAE values of $NHC_{GLM}1$ and $NHC_{GLM}2$ are 0.58 and 0.52, respectively, larger than those of $NHC_{GLA}1$ and $NHC_{GLA}2$ (0.27 and 0.10). Hence, the adverse effects of NHCs on human health are enhanced with the increasing number of methyl groups in RNSs.

To better understand the adverse health effects of NHCs, the PAE values of phthalates and polycyclic aromatic hydrocarbons (PAHs), which are well-known for their adverse health effects, are also calculated as a reference and depicted in Figure S21. Herein, dimethyl phthalate (DMP), diethyl phthalate (DEP), dipropyl phthalate (DPP), and dibutyl phthalate (DBP) are chosen as the models of phthalates, and naphthalene (NA), anthracene (AN), and 1,2-benzopyrene (BE) are selected as PAH models. As shown in Figure S21, the PAE values for the target phthalates and PAHs on the lungs range from 0.12 to 0.18 and 0.09 to 0.97, respectively, and those for NHCs range from 0.06 to 0.79. It implies that NHCs exhibit PAE values on the lungs similar to those of phthalates and PAHs.

■ ENVIRONMENTAL IMPLICATIONS

This study provides systematic insights into the formation of BrC from the aqueous-phase reactions of MG with three target RNSs (MA, DA, and AM) from combined quantum chemical calculations and laboratory experiments and also reveals the effects of the methyl groups on the oligomerization mechanism, product distribution, and light absorption of the products. Our findings indicate that (i) DIMI formation is regulated by the number of methyl groups in RNSs because excessive methyl groups occupy the reactive sites of amino groups, leading to the absence of the deprotonation reaction, (ii) the ability of NHC formation is controlled by the electrostatic attraction and steric hindrance of the methyl groups in RNSs, (iii) electrostatic attraction is weakened when the number of methyl groups in RNSs is increased, and (iv) the aqueous−phase reactions of small α-dicarbonyls with secondary amine do not form NHCs, but their contribution to SOA cannot be ignored.

To further assess the impact of the environmental pH on NHC formation, we also identified the chemical compositions at pH 3 and 5 for the three target reaction systems. The spectra of MG + MA, MG + DA, and MG + AM with EICs are shown in Figures S16b,c, S17, and S22. And the detailed peak assignments are shown in Table S7. As discussed in the SI, the same chemical composition is observed at pH 3 and 5 for the three target reaction systems. It suggests that there is little effect of pH on the major products in the MG + RNSs reaction systems under acidic conditions, which is consistent with the recent experimental result.[77] However, under alkaline conditions, BrC chromophores are yielded from the aqueous-phase reactions of MG and DA,[26] contrary to the formation of N-containing chain oligomers under acidic conditions. It indicates that the formation of BrC chromophores depends on the acidic conditions in fine aerosols and cloud/fog droplets.

On the other hand, to further explore the effect of the methyl groups on NHCs, we also calculated the UV−vis absorption spectra of the four additional typical NHCs in the GL + RNSs (RNSs = MA and AM) reaction systems (Figure 6d) and also assessed their light absorption abilities with the six NHCs obtained in this study. Similar to the MG + RNSs reaction systems, the NHCs ($NHC_{GLM}1$ and $NHC_{GLA}1$) with large planarity in the side chain (Figure S19) exhibit a high conjugative degree, contributing to obvious BrC absorption. However, for the NHCs (i.e., $NHC_{GLM}2$ and $NHC_{GLA}2$) with hydroxyl groups in the side chain, the calculated spectra are in the range of 200−235 nm, with no light absorption beyond 255 nm. For four strong light absorption NHCs (i.e., $NHC_{MGM}1$, $NHC_{MGA}1$, $NHC_{GLM}1$, and $NHC_{GLA}1$), the light absorption of NHCs from AM reaction systems (i.e., $NHC_{MGA}1$ and $NHC_{GLA}1$) is stronger than those from MA reaction systems ($NHC_{MGM}1$ and $NHC_{GLM}1$). It indicates that the number of the methyl groups in RNSs hinders light absorption of NHCs in the BrC region. Hence, our results indicate that BrC aerosols, if formed from the heterogeneous reactions of MG + RNSs, are likely affected by environmental acidity and the number of methyl groups in RNSs. Our mechanisms may be more applicable to urban environments due to the high abundance of RNSs and MG and the variety of RNSs, and our results provide the fundamental kinetic and mechanistic data for incorporating these mechanisms into atmospheric models to

assess the impacts of aerosols on air quality, human health, and climate.

■ ASSOCIATED CONTENT

ⓈI Supporting Information

The Supporting Information is available free of charge at https://pubs.acs.org/doi/10.1021/acs.est.3c05983.

> The relaxed potential energy curves; UV−vis absorption spectra; potential energy surfaces and optimized geometries; natural bond orbitals; planarity of all N-heterocycles; rate constants of MG oligomerization; mass spectra; probability of adverse effects; chemical formula and proposed chemical structures (PDF)

■ AUTHOR INFORMATION

Corresponding Author

Yuemeng Ji − *Guangdong Key Laboratory of Environmental Catalysis and Health Risk Control, Guangdong-Hong Kong−Macao Joint Laboratory for Contaminants Exposure and Health, Institute of Environmental Health and Pollution Control, Guangdong University of Technology, Guangzhou 510006, China; Guangzhou Key Laboratory of Environmental Catalysis and Pollution Control, Key Laboratory for City Cluster Environmental Safety and Green Development of the Ministry of Education, School of Environmental Science and Engineering, Guangdong University of Technology, Guangzhou 510006, China;* ⓞ orcid.org/0000-0002-8641-4276; Email: jiym@gdut.edu.cn

Authors

Qiuju Shi − *Guangdong Key Laboratory of Environmental Catalysis and Health Risk Control, Guangdong-Hong Kong−Macao Joint Laboratory for Contaminants Exposure and Health, Institute of Environmental Health and Pollution Control, Guangdong University of Technology, Guangzhou 510006, China; Guangzhou Key Laboratory of Environmental Catalysis and Pollution Control, Key Laboratory for City Cluster Environmental Safety and Green Development of the Ministry of Education, School of Environmental Science and Engineering, Guangdong University of Technology, Guangzhou 510006, China*

Lei Gao − *Guangdong Key Laboratory of Environmental Catalysis and Health Risk Control, Guangdong-Hong Kong−Macao Joint Laboratory for Contaminants Exposure and Health, Institute of Environmental Health and Pollution Control, Guangdong University of Technology, Guangzhou 510006, China; Guangzhou Key Laboratory of Environmental Catalysis and Pollution Control, Key Laboratory for City Cluster Environmental Safety and Green Development of the Ministry of Education, School of Environmental Science and Engineering, Guangdong University of Technology, Guangzhou 510006, China*

Wenjian Li − *Guangdong Key Laboratory of Environmental Catalysis and Health Risk Control, Guangdong-Hong Kong−Macao Joint Laboratory for Contaminants Exposure and Health, Institute of Environmental Health and Pollution Control, Guangdong University of Technology, Guangzhou 510006, China; Guangzhou Key Laboratory of Environmental Catalysis and Pollution Control, Key Laboratory for City Cluster Environmental Safety and Green Development of the Ministry of Education, School of Environmental Science and Engineering, Guangdong University of Technology, Guangzhou*

510006, China

Jiaxin Wang − *Guangdong Key Laboratory of Environmental Catalysis and Health Risk Control, Guangdong-Hong Kong−Macao Joint Laboratory for Contaminants Exposure and Health, Institute of Environmental Health and Pollution Control, Guangdong University of Technology, Guangzhou 510006, China; Guangzhou Key Laboratory of Environmental Catalysis and Pollution Control, Key Laboratory for City Cluster Environmental Safety and Green Development of the Ministry of Education, School of Environmental Science and Engineering, Guangdong University of Technology, Guangzhou 510006, China*

Zhang Shi − *Guangdong Key Laboratory of Environmental Catalysis and Health Risk Control, Guangdong-Hong Kong−Macao Joint Laboratory for Contaminants Exposure and Health, Institute of Environmental Health and Pollution Control, Guangdong University of Technology, Guangzhou 510006, China; Guangzhou Key Laboratory of Environmental Catalysis and Pollution Control, Key Laboratory for City Cluster Environmental Safety and Green Development of the Ministry of Education, School of Environmental Science and Engineering, Guangdong University of Technology, Guangzhou 510006, China*

Yixin Li − *Department of Chemistry, University of California Irvine, Irvine, California 92697, United States*

Jiangyao Chen − *Guangdong Key Laboratory of Environmental Catalysis and Health Risk Control, Guangdong-Hong Kong−Macao Joint Laboratory for Contaminants Exposure and Health, Institute of Environmental Health and Pollution Control, Guangdong University of Technology, Guangzhou 510006, China; Guangzhou Key Laboratory of Environmental Catalysis and Pollution Control, Key Laboratory for City Cluster Environmental Safety and Green Development of the Ministry of Education, School of Environmental Science and Engineering, Guangdong University of Technology, Guangzhou 510006, China;* ⓞ orcid.org/0000-0003-1491-2257

Taicheng An − *Guangdong Key Laboratory of Environmental Catalysis and Health Risk Control, Guangdong-Hong Kong−Macao Joint Laboratory for Contaminants Exposure and Health, Institute of Environmental Health and Pollution Control, Guangdong University of Technology, Guangzhou 510006, China; Guangzhou Key Laboratory of Environmental Catalysis and Pollution Control, Key Laboratory for City Cluster Environmental Safety and Green Development of the Ministry of Education, School of Environmental Science and Engineering, Guangdong University of Technology, Guangzhou 510006, China;* ⓞ orcid.org/0000-0001-6918-8070

Complete contact information is available at:
https://pubs.acs.org/10.1021/acs.est.3c05983

Author Contributions

∥These two authors contributed equally to this work.

Notes

The authors declare no competing financial interest.

■ ACKNOWLEDGMENTS

◼ REFERENCES

(1) Chowdhury, P. H.; He, Q.; Lasitza Male, T.; Brune, W. H.; Rudich, Y.; Pardo, M. Exposure of lung epithelial cells to photochemically aged secondary organic aerosol shows increased toxic effects. *Environ. Sci. Technol. Lett.* **2018**, *5*, 424−430.

(2) Millman, A.; Tang, D.; Perera, F. P. Air pollution threatens the health of children in China. *Pediatrics* **2008**, *122*, 620−628.

(3) Pye, H. O. T.; Ward Caviness, C. K.; Murphy, B. N.; Appel, K. W.; Seltzer, K. M. Secondary organic aerosol association with cardiorespiratory disease mortality in the United States. *Nat. Commun.* **2021**, *12*, 7215.

(4) Chowdhury, S.; Pozzer, A.; Haines, A.; Klingmuller, K.; Munzel, T.; Paasonen, P.; Sharma, A.; Venkataraman, C.; Lelieveld, J. Global health burden of ambient PM2.5 and the contribution of anthropogenic black carbon and organic aerosols. *Environ. Int.* **2022**, *159*, No. 107020.

(5) Xiang, W.; Wang, W.; Du, L.; Zhao, B.; Liu, X.; Zhang, X.; Yao, L.; Ge, M. Toxicological effects of secondary air pollutants. *Chem. Res. Chin. Univ.* **2023**, *39*, 326−341.

(6) Zhuang, X.; Wang, Y.; He, H.; Liu, J.; Wang, X.; Zhu, T.; Ge, M.; Zhou, J.; Tang, G.; Ma, J. Haze insights and mitigation in China: an overview. *J. Environ. Sci. (China).* **2014**, *26*, 2−12.

(7) Chen, H.; Yan, C.; Fu, Q.; Wang, X.; Tang, J.; Jiang, B.; Sun, H.; Luan, T.; Yang, Q.; Zhao, Q.; Li, J.; Zhang, G.; Zheng, M.; Zhou, X.; Chen, B.; Du, L.; Zhou, R.; Zhou, T.; Xue, L. Optical properties and molecular composition of wintertime atmospheric water-soluble organic carbon in different coastal cities of eastern China. *Sci. Total Environ.* **2023**, *892*, No. 164702.

(8) Lin, Y.; Wang, Y.; Pan, B.; Hu, J.; Guo, S.; Levy Zamora, M.; Tian, P.; Su, Q.; Ji, Y.; Zhao, J.; Gomez Hernandez, M.; Hu, M.; Zhang, R. Formation, radiative forcing, and climatic effects of severe regional haze. *Atmos. Chem. Phys.* **2022**, *22*, 4951−4967.

(9) Zhang, R.; Wang, G.; Guo, S.; Zamora, M. L.; Ying, Q.; Lin, Y.; Wang, W.; Hu, M.; Wang, Y. Formation of urban fine particulate matter. *Chem. Rev.* **2015**, *115*, 3803−3855.

(10) Chung, C. E.; Ramanathan, V.; Decremer, D. Observationally constrained estimates of carbonaceous aerosol radiative forcing. *Proc. Natl. Acad. Sci. U. S. A.* **2012**, *109*, 11624−11629.

(11) Wang, X.; Heald, C. L.; Sedlacek, A. J.; de Sá, S. S.; Martin, S. T.; Alexander, M. L.; Watson, T. B.; Aiken, A. C.; Springston, S. R.; Artaxo, P. Deriving brown carbon from multiwavelength absorption measurements: method and application to AERONET and Aethalometer observations. *Atmos. Chem. Phys.* **2016**, *16*, 12733−12752.

(12) Feng, Y.; Ramanathan, V.; Kotamarthi, V. R. Brown carbon: a significant atmospheric absorber of solar radiation? *Atmos. Chem. Phys.* **2013**, *13*, 8607−8621.

(13) Wang, X.; Heald, C. L.; Ridley, D. A.; Schwarz, J. P.; Spackman, J. R.; Perring, A. E.; Coe, H.; Liu, D.; Clarke, A. D. Exploiting simultaneous observational constraints on mass and absorption to estimate the global direct radiative forcing of black carbon and brown carbon. *Atmos. Chem. Phys.* **2014**, *14*, 10989−11010.

(14) Jo, D. S.; Park, R. J.; Lee, S.; Kim, S. W.; Zhang, X. A global simulation of brown carbon: Implications for photochemistry and direct radiative effect. *Atmos. Chem. Phys.* **2016**, *16*, 3413−3432.

(15) You, B.; Li, S.; Tsona, N. T.; Li, J.; Xu, L.; Yang, Z.; Cheng, S.; Chen, Q.; George, C.; Ge, M.; Du, L. Environmental processing of short-chain fatty alcohols induced by photosensitized chemistry of brown carbons. *ACS Earth. Space Chem.* **2020**, *4*, 631−640.

(16) De Haan, D. O.; Hawkins, L. N.; Kononenko, J. A.; Turley, J. J.; Corrigan, A. L.; Tolbert, M. A.; Jimenez, J. L. Formation of nitrogen-containing oligomers by methylglyoxal and amines in simulated evaporating cloud droplets. *Environ. Sci. Technol.* **2011**, *45*, 984−991.

(17) Lee, A. K.; Zhao, R.; Li, R.; Liggio, J.; Li, S. M.; Abbatt, J. P. Formation of light absorbing organo-nitrogen species from evaporation of droplets containing glyoxal and ammonium sulfate. *Environ. Sci. Technol.* **2013**, *47*, 12819−12826.

(18) Nozière, B.; Dziedzic, P.; Córdova, A. Formation of secondary light-absorbing "fulvic-like" oligomers: A common process in aqueous and ionic atmospheric particles? *Geophys. Res. Lett.* **2007**, *34*, No. L21812.

(19) Li, S.; Jiang, X.; Roveretto, M.; George, C.; Liu, L.; Jiang, W.; Zhang, Q.; Wang, W.; Ge, M.; Du, L. Photochemical aging of atmospherically reactive organic compounds involving brown carbon at the air−aqueous interface. *Atmos. Chem. Phys.* **2019**, *19*, 9887−9902.

(20) Drozd, G. T.; McNeill, V. F. Organic matrix effects on the formation of light-absorbing compounds from alpha-dicarbonyls in aqueous salt solution. *Environ. Sci. Process Impacts* **2014**, *16*, 741−747.

(21) De Haan, D. O.; Hawkins, L. N.; Wickremasinghe, P. D.; Andretta, A. D.; Dignum, J. R.; De Haan, A. C.; Welsh, H. G.; Pennington, E. A.; Cui, T.; Surratt, J. D.; Cazaunau, M.; Pangui, E.; Doussin, J. F. Brown carbon from photo-oxidation of glyoxal and SO₂ in Aqueous Aerosol. *ACS Earth. Space Chem.* **2023**, *7*, 1131−1140.

(22) Yang, Z.; Tsona, N. T.; George, C.; Du, L. Nitrogen-containing compounds enhance light absorption of aromatic-derived brown carbon. *Environ. Sci. Technol.* **2022**, *56*, 4005−4016.

(23) Hamilton, J. F.; Baeza-Romero, M. T.; Finessi, E.; Rickard, A. R.; Healy, R. M.; Peppe, S.; Adams, T. J.; Daniels, M. J.; Ball, S. M.; Goodall, I. C.; Monks, P. S.; Borras, E.; Munoz, A. Online and offline mass spectrometric study of the impact of oxidation and ageing on glyoxal chemistry and uptake onto ammonium sulfate aerosols. *Faraday Discuss.* **2013**, *165*, 447−472.

(24) Laskin, A.; Laskin, J.; Nizkorodov, S. A. Chemistry of atmospheric brown carbon. *Chem. Rev.* **2015**, *115*, 4335−4382.

(25) Qiu, C.; Zhang, R. Multiphase chemistry of atmospheric amines. *Phys. Chem. Chem. Phys.* **2013**, *15*, 5738−5752.

(26) Marrero-Ortiz, W.; Hu, M.; Du, Z.; Ji, Y.; Wang, Y.; Guo, S.; Lin, Y.; Gomez-Hermandez, M.; Peng, J.; Li, Y.; Secrest, J.; Zamora, M. L.; Wang, G.; An, T.; Zhang, R. Formation and optical properties of brown carbon from small α-dicarbonyls and amines. *Environ. Sci. Technol.* **2019**, *53*, 117−126.

(27) Li, Y.; Ji, Y.; Zhao, J.; Wang, Y.; Shi, Q.; Peng, J.; Wang, Y.; Wang, C.; Zhang, F.; Wang, Y.; Seinfeld, J. H.; Zhang, R. Unexpected oligomerization of small alpha-dicarbonyls for secondary organic aerosol and brown carbon formation. *Environ. Sci. Technol.* **2021**, *55*, 4430−4439.

(28) De Haan, D. O.; Hawkins, L. N.; Welsh, H. G.; Pednekar, R.; Casar, J. R.; Pennington, E. A.; de Loera, A.; Jimenez, N. G.; Symons, M. A.; Zauscher, M.; Pajunoja, A.; Caponi, L.; Cazaunau, M.; Formenti, P.; Gratien, A.; Pangui, E.; Doussin, J. F. Brown carbon production in ammonium- or amine-containing aerosol particles by reactive uptake of methylglyoxal and photolytic cloud cycling. *Environ. Sci. Technol.* **2017**, *51*, 7458−7466.

(29) Sareen, N.; Waxman, E. M.; Turpin, B. J.; Volkamer, R.; Carlton, A. G. Potential of Aerosol Liquid Water to Facilitate organic aerosol formation: assessing knowledge gaps about precursors and partitioning. *Environ. Sci. Technol.* **2017**, *51*, 3327−3335.

(30) Hallquist, M.; Wenger, J. C.; Baltensperger, U.; Rudich, Y.; Simpson, D.; Claeys, M.; Dommen, J.; Donahue, N. M.; George, C.; Goldstein, A. H.; Hamilton, J. F.; Herrmann, H.; Hoffmann, T.; Iinuma, Y.; Jang, M.; Jenkin, M. E.; Jimenez, J. L.; Kiendler-Scharr, A.; Maenhaut, W.; McFiggans, G.; Mentel, T. F.; Monod, A.; Prevot, A. S. H.; Seinfeld, J. H.; Surratt, J. D.; Szmigielski, R.; Wildt, J. The formation, properties and impact of secondary organic aerosol: current and emerging issues. *Atmos. Chem. Phys.* **2009**, *9*, 5155−5236.

(31) Fu, T. M.; Jacob, D. J.; Wittrock, F.; Burrows, J. P.; Vrekoussis, M.; Henze, D. K. Global budgets of atmospheric glyoxal and methylglyoxal, and implications for formation of secondary organic aerosols. *J. Geophys. Res.* **2008**, *113*, No. D15303.

(32) Kroll, J. H.; Ng, N. L.; Murphy, S. M.; Varutbangkul, V.; Flagan, R. C.; Seinfeld, J. H. Chamber studies of secondary organic aerosol growth by reactive uptake of simple carbonyl compounds. *J. Geophys. Res.: Atmos.* **2005**, *110*, No. D23207.

(33) Zhao, J.; Levitt, N. P.; Zhang, R.; Chen, J. Heterogeneous reactions of methylglyoxal in acidic media: implications for secondary organic aerosol formation. *Environ. Sci. Technol.* **2006**, *40*, 7682−7687.

(34) Wang, L.; Xu, W.; Khalizov, A. F.; Zheng, J.; Qiu, C.; Zhang, R. Laboratory investigation on the role of organics in atmospheric nanoparticle growth. *J. Phys. Chem. A* **2011**, *115*, 8940−8947.

(35) Hamilton, J. F.; Rami Alfarra, M.; Wyche, K. P.; Ward, M. W.; Lewis, A. C.; McFiggans, G. B.; Good, N.; Monks, P. S.; Carr, T.; White, I. R.; Purvis, R. M. Investigating the use of secondary organic aerosol as seed particles in simulation chamber experiments. *Atmos. Chem. Phys.* **2011**, *11*, 5917−5929.

(36) De Haan, D. O.; Pajunoja, A.; Hawkins, L. N.; Welsh, H. G.; Jimenez, N. G.; De Loera, A.; Zauscher, M.; Andretta, A. D.; Joyce, B. W.; De Haan, A. C.; Riva, M.; Cui, T.; Surratt, J. D.; Cazaunau, M.; Formenti, P.; Gratien, A.; Pangui, E.; Doussin, J. F. Methylamine's effects on methylglyoxal-containing aerosol: chemical, physical, and optical changes. *ACS Earth. Space Chem.* **2019**, *3*, 1706−1716.

(37) Wong, J. P. S.; Nenes, A.; Weber, R. J. Changes in light absorptivity of molecular weight separated brown carbon due to photolytic aging. *Environ. Sci. Technol.* **2017**, *51*, 8414−8421.

(38) Zhao, R.; Lee, A. K. Y.; Huang, L.; Li, X.; Yang, F.; Abbatt, J. P. D. Photochemical processing of aqueous atmospheric brown carbon. *Atmos. Chem. Phys.* **2015**, *15*, 6087−6100.

(39) Ho, C. T.; Liu, S.; Li, S. Safety issues of methylglyoxal and potential scavengers. *Front. Agric. Sci. Eng.* **2018**, *5*, 312−320.

(40) Rabbani, N.; Xue, M.; Thornalley, P. J. Dicarbonyls and glyoxalase in disease mechanisms and clinical therapeutics. *Glycoconj. J.* **2016**, *33*, 513−525.

(41) Ji, Y.; Shi, Q.; Li, Y.; An, T.; Zheng, J.; Peng, J.; Gao, Y.; Chen, J.; Li, G.; Wang, Y.; Zhang, F.; Zhang, A. L.; Zhao, J.; Molina, M. J.; Zhang, R. Carbenium ion-mediated oligomerization of methylglyoxal for secondary organic aerosol formation. *Proc. Natl. Acad. Sci. U. S. A.* **2020**, *117*, 13294−13299.

(42) Chen, Q.; Wang, M.; Wang, Y.; Zhang, L.; Li, Y.; Han, Y. Oxidative potential of water-soluble matter associated with chromophoric substances in PM2.5 over Xi'an, China. *Environ. Sci. Technol.* **2019**, *53*, 8574−8584.

(43) Zhang, T.; Huang, S.; Wang, D.; Sun, J.; Zhang, Q.; Xu, H.; Hang Ho, S. S.; Cao, J.; Shen, Z. Seasonal and diurnal variation of PM2.5 HULIS over Xi'an in Northwest China: Optical properties, chemical functional group, and relationship with reactive oxygen species (ROS). *Atmos. Environ.* **2022**, *268*, No. 118782.

(44) Cho, A. K.; Sioutas, C.; Miguel, A. H.; Kumagai, Y.; Schmitz, D. A.; Singh, M.; Eiguren-Fernandez, A.; Froines, J. R. Redox activity of airborne particulate matter at different sites in the Los Angeles Basin. *Environ. Res.* **2005**, *99*, 40−47.

(45) Brook, R. D.; Rajagopalan, S.; Pope, C. A.; Brook, J. R.; Bhatnagar, A.; Diez-Roux, A. V.; Holguin, F.; Hong, Y.; Luepker, R. V.; Mittleman, M. A.; Peters, A.; Siscovick, D.; Smith, S. C.; Whitsel, L.; Kaufman, J. D. Particulate matter air pollution and cardiovascular disease: An update to the scientific statement from the American Heart Association. *Circulation* **2010**, *121*, 2331−2378.

(46) Bates, J. T.; Fang, T.; Verma, V.; Zeng, L.; Weber, R. J.; Tolbert, P. E.; Abrams, J. Y.; Sarnat, S. E.; Klein, M.; Mulholland, J. A.; Russell, A. G. Review of Acellular assays of ambient particulate matter oxidative potential: methods and relationships with composition, sources, and health effects. *Environ. Sci. Technol.* **2019**, *53*, 4003−4019.

(47) Lin, P.; Laskin, J.; Nizkorodov, S. A.; Laskin, A. Revealing brown carbon chromophores produced in reactions of methylglyoxal with ammonium sulfate. *Environ. Sci. Technol.* **2015**, *49* (24), 14257−14266.

(48) De Haan, D. O.; Tapavicza, E.; Riva, M.; Cui, T.; Surratt, J. D.; Smith, A. C.; Jordan, M. C.; Nilakantan, S.; Almodovar, M.; Stewart, T. N.; de Loera, A.; De Haan, A. C.; Cazaunau, M.; Gratien, A.; Pangui, E.; Doussin, J. F. Nitrogen-containing, light-absorbing oligomers produced in aerosol particles exposed to methylglyoxal, photolysis, and cloud cycling. *Environ. Sci. Technol.* **2018**, *52*, 4061−4071.

(49) Hawkins, L. N.; Welsh, H. G.; Alexander, M. V. Evidence for pyrazine-based chromophores in cloud water mimics containing methylglyoxal and ammonium sulfate. *Atmos. Chem. Phys.* **2018**, *18*, 12413−12431.

(50) Frisch, M. J.; Trucks, G. W.; Schlegel, H. B.; Scuseria, G. E.; Robb, M. A.; Cheeseman, J. R.; Scalmani, G.; Barone, V.; Mennucci, B.; Petersson, G. A.; Nakatsuji, H.; Caricato, M.; Li, X.; Hratchian, H. P.; Izmaylov, A. F.; Bloino, J.; Zheng, G.; Sonnenberg, J. L.; Hada, M.; Ehara, M.; Toyota, K.; Fukuda, R.; Hasegawa, J.; Ishida, M.; Nakajima, T.; Honda, Y.; Kitao, O.; Nakai, H.; Vreven, T.; Montgomery, J. A.; Peralta, J. E.; Ogliaro, F.; Bearpark, M.; Heyd, J. J.; Brothers, E.; Kudin, K. N.; Staroverov, V. N.; Keith, T.; Kobayashi, R.; Normand, J.; Raghavachari, K.; Rendell, A.; Burant, J. C.; Iyengar, S. S.; Tomasi, J.; Cossi, M.; Rega, N.; Millam, J. M.; Klene, M.; Knox, J. E.; Cross, J. B.; Bakken, V.; Adamo, C.; Jaramillo, J.; Gomperts, R.; Stratmann, R. E.; Yazyev, O.; Austin, A. J.; Cammi, R.; Pomelli, C.; Ochterski, J. W.; Martin, R. L.; Morokuma, K.; Zakrzewski, V. G.; Voth, G. A.; Salvador, P.; Dannenberg, J. J.; Dapprich, S.; Daniels, A. D.; Farkas, Ö.; Foresman, J. B.; Ortiz, J. V.; Cioslowski, J.; Fox, D. J. *Gaussian 09*, Revision D.01; Gaussian, Inc.: Wallingford CT, 2009.

(51) Zhao, Y.; Truhlar, D. G. The M06 suite of density functionals for main group thermochemistry, thermochemical kinetics, noncovalent interactions, excited states, and transition elements: two new functionals and systematic testing of four M06-class functionals and 12 other functionals. *Theor. Chem. Acc.* **2008**, *120*, 215−241.

(52) Ji, Y.; Zhao, J.; Terazono, H.; Misawa, K.; Levitt, N. P.; Li, Y.; Lin, Y.; Peng, J.; Wang, Y.; Duan, L.; Pan, B.; Zhang, F.; Feng, X.; An, T.; Marrero-Ortiz, W.; Secrest, J.; Zhang, A. L.; Shibuya, K.; Molina, M. J.; Zhang, R. Reassessing the atmospheric oxidation mechanism of toluene. *Proc. Natl. Acad. Sci. U. S. A.* **2017**, *114*, 8169−8174.

(53) Shi, Q.; Zhang, W.; Ji, Y.; Wang, J.; Qin, D.; Chen, J.; Gao, Y.; Li, G.; An, T. Enhanced uptake of glyoxal at the acidic nanoparticle interface: implications for secondary organic aerosol formation. *Environ. Sci.: Nano* **2020**, *7*, 1126−1135.

(54) Ji, Y.; Shi, Q.; Ma, X.; Gao, L.; Wang, J.; Li, Y.; Gao, Y.; Li, G.; Zhang, R.; An, T. Elucidating the critical oligomeric steps in secondary organic aerosol and brown carbon formation. *Atmos. Chem. Phys.* **2022**, *22*, 7259−7271.

(55) Marenich, A. V.; Cramer, C. J.; Truhlar, D. G. Universal solvation model based on solute electron density and on a continuum model of the solvent defined by the bulk dielectric constant and atomic surface tensions. *J. Phys. Chem. B* **2009**, *113*, 6378−6396.

(56) Hazra, M. K.; Sinha, A. Formic acid catalyzed hydrolysis of SO_3 in the gas phase: a barrierless mechanism for sulfuric acid production of potential atmospheric importance. *J. Am. Chem. Soc.* **2011**, *133*, 17444−17453.

(57) Glendening, E. D.; Landis, C. R.; Weinhold, F. Natural bond orbital methods. *Wires Comput. Mol. Sci.* **2012**, *2*, 1−42.

(58) Eyring, H. The Activated complex in chemical reactions. *J. Chem. Phys.* **1935**, *3*, 107−115.

(59) Evans, M. G.; Polanyi, M. Some applications of the transition state method to the calculation of reaction velocities, especially in solution. *Trans. Fara. Soc.* **1935**, *31*, 875−894.

(60) Gao, Y.; Ji, Y.; Li, G.; An, T. Mechanism, kinetics and toxicity assessment of OH-initiated transformation of triclosan in aquatic environments. *Wat. Res.* **2014**, *49*, 360−370.

(61) Okuno, Y. Theoretical investigation of the mechanism of the baeyer-villiger reaction in nonpolar solvents. *Chem.- Eur. J.* **1997**, *3*, 212−218.

(62) Collins, F. C.; Kimball, G. E. Diffusion-controlled reaction rates. *J. Colloid. Sci.* **1949**, *4*, 425−437.

(63) Bauernschmitt, R.; Ahlrichs, R. Treatment of electronic excitations within the adiabatic approximation of time dependent density functional theory. *Chem. Phys. Lett.* **1996**, *256*, 454−464.

(64) Lin, P.; Liu, J.; Shilling, J. E.; Kathmann, S. M.; Laskin, J.; Laskin, A. Molecular characterization of brown carbon (BrC) chromophores in secondary organic aerosol generated from photo-oxidation of toluene. *Phys. Chem. Chem. Phys.* **2015**, *17*, 23312−23325.

(65) Fleming, S.; Mills, A.; Tuttle, T. Predicting the UV-vis spectra of oxazine dyes. *Beilstein J. Org. Chem.* **2011**, *7*, 432−441.

(66) Chen, J. Y.; Rodriguez, E.; Jiang, H.; Chen, K.; Frie, A.; Zhang, H.; Bahreini, R.; Lin, Y. H. Time-dependent density functional theory investigation of the uv−vis spectra of organonitrogen chromophores in brown carbon. *ACS Earth Space Chem.* **2020**, *4*, 311−320.

(67) Calvert, C. T.; Schnitzler, E. G. Light absorption by cinnamaldehyde constituents of biomass burning organic aerosol modeled using time-dependent density functional theory. *ACS Earth Space Chem.* **2023**, *7*, 490−500.

(68) Grace, D. N.; Sharp, J. R.; Holappa, R. E.; Lugos, E. N.; Sebold, M. B.; Griffith, D. R.; Hendrickson, H. P.; Galloway, M. M. Heterocyclic product formation in aqueous brown carbon systems. *ACS Earth. Space Chem.* **2019**, *3*, 2472−2481.

(69) Ziegler, T.; Krykunov, M.; Cullen, J. The application of constricted variational density functional theory to excitations involving electron transitions from occupied lone-pair orbitals to virtual pi* orbitals. *J. Chem. Theory. Comput.* **2011**, *7*, 2485−2491.

(70) Jacquemin, D.; Moore, B.; Planchat, A.; Adamo, C.; Autschbach, J. Performance of an optimally tuned range-separated hybrid functional for 0−0 electronic excitation energies. *J. Chem. Theory Comput.* **2014**, *10*, 1677−1685.

(71) Lu, T.; Chen, F. Multiwfn: A multifunctional wavefunction analyzer. *J. Comput. Chem.* **2012**, *33*, 580−592.

(72) Lu, T. Simple, reliable, and universal metrics of molecular planarity. *J. Mol. Model.* **2021**, *27* (9), 263.

(73) Wang, X.; Hayeck, N.; Brüggemann, M.; Yao, L.; Chen, H.; Zhang, C.; Emmelin, C.; Chen, J.; George, C.; Wang, L. Chemical characteristics of organic aerosols in shanghai: a study by ultrahigh-performance liquid chromatography coupled with orbitrap mass spectrometry. *J. Geophys. Res.: Atmos.* **2017**, *122*, 11703−11722.

(74) Wang, M.; Gao, Y.; Li, G.; An, T. Increased adverse effects during metabolic transformation of short-chain chlorinated paraffins by cytochrome P450: A theoretical insight into 1-chlorodecane. *J. Hazard. Mater.* **2021**, *407*, No. 124391.

(75) Advanced Chemistry Development. *ACD/Percepta*; ACD/Labs Percepta, Inc.: Toronto, Ontario, Canada, 2016.

(76) Gawlik, M.; Trawinski, J.; Skibinski, R. Identification and characterization of citalopram new metabolites with the use of UHPLC-Q-TOF technique: In silico toxicity assessment of the identified transformation products. *J. Pharm. Biomed. Anal.* **2020**, *186*, No. 113299.

(77) Yang, L.; Huang, R.-J.; Shen, J.; Wang, T.; Gong, Y.; Yuan, W.; Liu, Y.; Huang, H.; You, Q.; Huang, D. D.; Huang, C. New insights into the brown carbon chromophores and formation pathways for aqueous reactions of α-dicarbonyls with amines and ammonium. *Environ. Sci. Technol.* **2023**, *57*, 12351−12361.

📖 Recommended by ACS